Alignment effects in two-photon double ionization of H_{2} in femtosecond xuv laser pulses

Xiaoxu Guan, Klaus Bartschat, and Barry I. Schneider

Phys. Rev. A **84**, 033403 — Published 6 September 2011

DOI: 10.1103/PhysRevA.84.033403

Alignment effects in two-photon double ionization of H_2 in femtosecond xuv laser pulses

Xiaoxu Guan[1], Klaus Bartschat[1], and Barry I. Schneider[2]
[1] *Department of Physics and Astronomy, Drake University, Des Moines, Iowa 50311, USA and*
[2] *Office of Cyberinfrastructure, National Science Foundation, Arlington, Virgina 22230, USA*

Triple-differential cross sections for two-photon double ionization of the aligned hydrogen molecule at the equilibrium distance are presented for a central photon energy of 30 eV. The temporal response of the laser-driven molecule is investigated by solving the time-dependent Schrödinger equation in full dimensionality using two-center elliptical coordinates and a finite-element discrete-variable-representation approach. The molecular orientation is found to have a strong effect on the emission modes of the two correlated photoelectrons. This molecular effect is most noticeable when the molecular axis and the laser polarization vector are oriented parallel to each other. For intermediate cases between the parallel and perpendicular geometries, the dominant emission modes for two-electron ejection oscillate between those for the two extreme cases. The contributions from different ionization channels are also analyzed in detail. Depending on the emission direction of the reference electron, the interference contributions from the various channels can be constructive or destructive at small alignment angles, while they always contribute constructively to the triple-differential cross sections near the perpendicular geometry.

PACS numbers: 33.80.-b, 33.80.Wz, 31.15.A-

I. INTRODUCTION

The goal of exploring multi-center effects, which are not present in atomic targets, has stimulated recent theoretical interest in the few-photon double ionization of molecules. The interest has further increased in light of the rapid developments in intense free-electron laser sources and imaging techniques in the xuv regime. Angular distributions in the complete breakup reaction of the hydrogen (or deuteron) "fixed-in-space" molecule by single-photon absorption were intensively studied on both experimental [1–3] and theoretical [4–6] fronts. The orientation of diatomic molecules can be determined through the relative momentum of the dissociated nuclear fragments during the short time interval when the electrons are removed [3]. This allows for a detailed exploration of the intricate emission modes of two correlated photoelectrons in a preset orientation of the molecular axis ($\boldsymbol{\zeta}$) and the linear laser polarization vector ($\boldsymbol{\epsilon}$).

Although only the nuclear fragments can be recorded experimentally for the nonlinear two-photon double ionization so far [7], tracking the ejected photoelectron signal is on the horizon. Theoretically, the two-photon nonsequential double ionization of "fixed in space" H_2 in the xuv regime ($\hbar\omega = 30$ eV) has concentrated on two particular geometries [8–10], in which the $\boldsymbol{\zeta}$ and $\boldsymbol{\epsilon}$ are either parallel or perpendicular to each other. Recently, the time-dependent close-coupling method [11] was also extended to study the two-photon sequential double ionization by laser pulses with peak intensities up to 10^{16} W/cm^2 at a central photon energy of 40 eV, but no alignment effects were studied.

The contributing partial-wave symmetries for the double-ionization channel are, respectively, $^1\Sigma_g$ for the parallel geometry, and $^1\Sigma_g$ and $^1\Delta_g$ for the perpendicular case. Based on previous investigations of these two extreme cases, the double-ionization signal in the perpendicular geometry in the xuv regime is predicted to be nearly ten times stronger than that for the parallel geometry. Consequently, one may wonder how the differential cross section evolves from a relatively small quantity in the parallel geometry to generally much larger average values in the perpendicular geometry.

When the alignment angle (θ_N) between the $\boldsymbol{\zeta}$ and $\boldsymbol{\epsilon}$ vectors is neither 0° (parallel geometry) nor 90° (perpendicular geometry), an additional ionization channel, namely the $^1\Pi_g$ contribution, needs to be taken into account in order to describe the dynamics of the photoelectrons emitted from the two-center diatomic target. The various ionization paths can be represented as

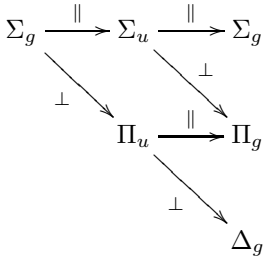

for $0° \leqslant \theta_N \leqslant 90°$, where $\parallel$ and $\perp$ represent the parallel and perpendicular components of the electric field, respectively.

The calculated angular distributions for $\theta_N = 0°$ and 90° essentially exhibit either a one-lobe or two-lobe structure. If θ_N is neither 0° nor 90°, however, one might ask whether the Π_g ionization channel would introduce any new structure in the angular distributions. Unlike the Σ_g or Δ_g channels, the Π_g channel in the two-photon process emerges from two paths: $\Sigma_g \xrightarrow{\parallel} \Sigma_u \xrightarrow{\perp} \Pi_g$ and $\Sigma_g \xrightarrow{\perp} \Pi_u \xrightarrow{\parallel} \Pi_g$. In other words, the appearance of

the Π_g channel is the result of combined parallel and perpendicular components of the electric field.

These intricacies provided the principal motivation for us to consider the more complicated interference effect between the three coupled ionization channels. Recall that these effects do not exist in the atomic counterpart, i.e., the helium atom. As an aside, we also investigate the contributions from each individual channel.

In this work, we focus our attention on the triple-differential cross section (TDCS) for two-photon double ionization of the H_2 molecule at a central photon energy of 30 eV, with emphasis on an arbitrary orientation between the molecular axis and the linear polarization vector of the laser field. Due to the computational complexity involved in this two-center two-electron system, we treat the problem in the fixed-nuclei approximation (FNA), in which the internuclear separation (R) is fixed at its equilibrium distance of 1.4 bohr. The double-ionization threshold at $R = 1.4$ bohr is about 51.4 eV above the initial electronic Σ_g state, while the single-ionization threshold is about 16.45 eV. At the photon energy of 30 eV, therefore, this is essentially a *direct* or nonsequential process.

We discretize the two-center molecular system in prolate spheroidal coordinates by employing a finite-element discrete variable representation (FE-DVR). The angle-differential cross section is extracted by solving the time-dependent Schrödinger equation (TDSE) on the preset mesh points and projecting the solution to uncoupled molecular Coulomb functions. The appealing features of the prolate coordinate system were already revealed in the pioneering work of Bates, Öpik, and Poots [12] on the H_2^+ ion. Without attempting a comprehensive overview of its numerous implementations in treating diatomic molecules, we note that this coordinate system has been widely employed to capture the two-center characteristics. A few representative examples include one-photon and two-photon double ionization of H_2 [6, 10, 13], multiphoton absorption of the H_2^+ ion [14–17] and H_2 [18], and antiproton- and electron-impact ionization of H_2^+ [19, 20].

The remainder of this paper is organized as follows. We outline the theoretical treatment in Sec. II. After a brief presentation of the computational details in Sec. III, our predictions for two-photon double ionization for arbitrary alignment geometries are presented and discussed in Sec. IV. We finish with a short summary in Sec. V.

II. THEORETICAL FRAMEWORK

The prolate spheroidal ansatz employs elliptical coordinates. Hence it is a highly suitable choice to describe two-center diatomic molecules, if the two foci are placed at the two nuclei. This coordinate system naturally maintains the rotational symmetry of diatomic molecules around their molecular axis through the azimuthal angle $\varphi \in [0, 2\pi]$. The "radial" ξ and "angular" η coordinates are defined by

$$\xi_i = (r_{1i} + r_{2i})/R, \quad \text{and} \quad \eta_i = (r_{1i} - r_{2i})/R, \tag{1}$$

where r_{1i} and r_{2i} are the distances measured from the two nuclei to the electron "i" of interest, at the internuclear separation R. The field-free part of the Hamiltonian is then written as

$$\mathcal{H} = \mathcal{H}_1 + \mathcal{H}_2 + \frac{1}{r_{12}} \tag{2}$$

with the one-electron part given by

$$\mathcal{H}_i = -\frac{2}{R^2(\xi_i^2 - \eta_i^2)}\left[\frac{\partial}{\partial\xi_i}(\xi_i^2 - 1)\frac{\partial}{\partial\xi_i} + \frac{\partial}{\partial\eta_i}(1 - \eta_i^2)\frac{\partial}{\partial\eta_i}\right. \tag{3}$$
$$\left. + \frac{1}{(\xi_i^2 - 1)}\frac{\partial^2}{\partial^2\varphi_i} + \frac{1}{(1 - \eta_i^2)}\frac{\partial^2}{\partial\varphi_i^2}\right] - \frac{4\xi_i}{R(\xi_i^2 - \eta_i^2)}.$$

We then use the Neumann expansion to treat the electron-electron interaction $1/r_{12}$. It is given by

$$\frac{1}{r_{12}} = \frac{2}{R}\sum_{l=0}^{l_{\max}}\sum_{m=-l}^{l}(-1)^{|m|}(2l+1)\left(\frac{(l-|m|)!}{(l+|m|)!}\right)^2 \tag{4}$$
$$\times P_l^{|m|}(\xi_<)Q_l^{|m|}(\xi_>)P_l^{|m|}(\eta_1)P_l^{|m|}(\eta_2)e^{im(\varphi_1-\varphi_2)}.$$

Here $P_l^{|m|}(\xi)$ and $Q_l^{|m|}(\xi)$ are the "radial" regular and irregular Legendre functions for $\xi_{>(<)} = \max(\min)(\xi_1, \xi_2)$, respectively, while $P_l^{|m|}(\eta)$ is the "angular" Legendre function. As discussed in detail previously [6], the numerical implementation of the current Neumann expansion in prolate spheroidal coordinates is far from trivial.

If the angular parts (η, φ) are expanded in terms of spherical harmonics, all the necessary angular integrals can be evaluated analytically. However, this results in a non-unity overlap matrix in the TDSE. In order to use the well-developed standard Lanczos method to solve the TDSE, we therefore choose to discretize both the ξ and η variables. To regain the diagonal representation of all the potentials in the DVR basis, the matrix elements of $1/r_{12}$ are very effectively generated by solving a Poisson equation in prolate spheroidal coordinates [6].

Unlike expanding the angular part in terms of spherical harmonics, however, the truncation of the Neumann expansion ($l_{\max}$) must be tested carefully. The value of $l_{\max}$ needs to be properly chosen to minimize the uncertainties caused by the Gaussian quadratures for the higher-order terms in solving the Poisson equation. In this work, we use nine Gauss-Legendre points to discretize η, and hence we truncate the expansion at $l_{\max} = 10$. This allows us to produce an accurate description of the initial state. Since details of our numerical implementation of the FE-DVR approach and the Lanczos algorithm for the time evolution of the system can be found in Refs. [6, 21], they will not be repeated here.

Once the time-dependent wave packet has been obtained at the end of time evolution, the triple-differential cross section can be extracted by projecting the wave packet onto the two-electron continuum channels. These are constructed as two continuum states of the H_2^+ ion. The TDCS can then be expressed as

$$\frac{\mathrm{d}^3\sigma}{\mathrm{d}E_1\mathrm{d}\hat{\boldsymbol{k}}_1\mathrm{d}\hat{\boldsymbol{k}}_2} = \frac{1}{k_1k_2\cos^2\alpha}\Big(\frac{\omega}{I_0}\Big)^2\frac{1}{T_{\mathrm{eff}}^{(2)}}\int_0^{k_{\max}}\mathrm{d}k_1'\int_0^{k_1'}\mathrm{d}k_2' \times k_1'\delta(k_2'-k_1'\tan\alpha)\Big|\sum_{m_1\ell_1m_2\ell_2}(-i)^{\ell_1+\ell_2}e^{i\left(\Delta_{|m_1|\ell_1}+\Delta_{|m_2|\ell_2}\right)} \times \mathcal{Y}_{\ell_1m_1}(k_1',\hat{\boldsymbol{k}}_1)\mathcal{Y}_{\ell_2m_2}(k_2',\hat{\boldsymbol{k}}_2)\mathfrak{F}_{\ell_1m_1\ell_2m_2}(k_1',k_2')\Big|^2. \quad (5)$$

Here ω and I_0 are the central photon energy and the peak intensity of the laser pulse, respectively. Furthermore, $T_{\mathrm{eff}}^{(2)}$ denotes the *effective* two-photon interaction time. It is given by $T_{\mathrm{eff}}^{(2)} = (35/128)\tau$ for a sine-squared pulse envelope of duration τ.

The hyperangle $\alpha = \tan^{-1}(k_2/k_1)$ is introduced to specify the energy sharing of the two electrons emitted with vector momenta $\boldsymbol{k}_1$ and $\boldsymbol{k}_2$ and corresponding magnitude k_1 and k_2. In Eq. (5), $\Delta_{|m|\ell}$ and $\mathcal{Y}_{\ell m}(\boldsymbol{k})$ denote the two-center Coulomb phase shift and a prolate spheroidal harmonic (c.f. [6]). We recall the symmetry relation $\mathcal{Y}_{\ell m}(-\boldsymbol{k}) = (-1)^\ell\mathcal{Y}_{\ell m}(\boldsymbol{k})$ under the inversion operation. This is similar to the properties of the spherical harmonics. Consequently, only angular partial waves with *even* parity, i.e., $(-1)^{\ell_1+\ell_2} = +1$, need to be incorporated in Eq. (5) for two-photon double ionization.

At an arbitrary orientation between the $\boldsymbol{\zeta}$ and $\boldsymbol{\epsilon}$ axes, the formalism of Eq. (5) shows that the double-ionization amplitude for two-photon absorption becomes a coherent superposition of different ionization channels. In other words, the angular distribution (or the shape of the TDCS) is determined by

$$\frac{\mathrm{d}^3\sigma}{\mathrm{d}E_1\mathrm{d}\hat{\boldsymbol{k}}_1\mathrm{d}\hat{\boldsymbol{k}}_2} \propto \Big|f_{\Sigma_g\to\Sigma_u\to\Sigma_g} + f_{\Sigma_g\to(\Sigma_u,\Pi_u)\to\Pi_g} + f_{\Sigma_g\to\Pi_u\to\Delta_g}\Big|^2, \quad (6)$$

where $f_{\Sigma_g\to\Sigma_u\to\Sigma_g}$, $f_{\Sigma_g\to(\Sigma_u,\Pi_u)\to\Pi_g}$, and $f_{\Sigma_g\to\Pi_u\to\Delta_g}$ are the ionization amplitudes for the various paths listed above. This expression can be further expanded as the (incoherent) sum of the contributions from the pure Σ_g, Π_g, and Δ_g channels, plus their coherent interference terms.

III. COMPUTATIONAL DETAILS

In the FNA, the internuclear separation R is held fixed during the time evolution of the laser-driven H_2 wavepacket. If the ionization event is impulsive, the electrons will be far away when the nuclei begin to separate, evolving dynamically according to the Coulomb repulsion between the two protons. Essentially, the dynamical motion of the electrons and the nuclei are decoupled and the ionization of the electrons occurs at a fixed internuclear separation. Should this not be a valid approximation, it becomes necessary to treat the electronic and nuclear motion in a more sophisticated fashion. This problem has not been solved in full generality to date. Even if it were possible, the calculation would be computationally very expensive.

This paper, therefore, is focused on a different issue, namely the alignment effect in two-photon double ionization with a fixed value of $R = 1.4$ bohr. As such, the calculations needed for a direct comparison with experimental data, requiring averaging over several experimental parameters (see below) as well as the treatment of the dynamical motion of the nuclei, would go far beyond currently available resources. The present work is hence confined to the qualitative effects associated with the opening of a new channel.

We confine the ξ coordinate to a "radial" box of $\xi_{\max} = 150$. This is equivalent to a spatial box of $r_{\max} \simeq R\xi_{\max}/2 \simeq 105$ bohr, measured from the molecular center. In the calculations for the results shown below, we used a pulse of "10 + 2" optical cycles (o.c.) at the central photon energy of 30 eV. The peak intensity was generally fixed at 10^{14} W/cm^2, except for the examination of a possible dependence of the TDCS results on the laser intensity. The "10 + 2" o.c. pulse means that the laser pulse contains 10 full cycles and is followed by a 2-cycle field-free time evolution. For our present short ($\sim$ 1.6 fs) interaction with the laser, this box is sufficiently large to avoid any unphysical reflection from the edge of box.

In the expansion (5) of the wave packet, we cut the sum over the magnetic quantum numbers, m_1 and m_2, of the two electrons along the molecular axis to $|m_1|_{\max} = |m_2|_{\max} = 4$. The ξ coordinate is discretized by defining 289 Gauss-Radau and Gauss-Lobatto mesh points between 1 and $\xi_{\max}$, with an increasingly dense point distribution near the nuclear region. As mentioned above, nine Gauss-Legendre η points are used, and the Neumann expansion is truncated at $l_{\max} = 10$. With these parameters and $R = 1.4$ bohr, we obtain a ground-state energy of -1.8887324 atomic units (a.u.) through relaxing an initial guess of the wave function in imaginary time. In the present work, therefore, we employ an even more accurate description of the initial state as well as the time evolution of the wave packet compared to our earlier work [10]. Interested readers are referred to Ref. [6] for a detailed explanation regarding the relevant boundary conditions, the truncation of the Neumann expansion, and the solution to the Poisson equation.

IV. RESULTS AND DISCUSSIONS

A. Survival probability

For the (generalized) cross section to be well defined, we need to ensure that the depletion of the initial state is negligible at the end of the time evolution. We therefore first examine the survival probability ($P_{\rm surv}$) at the central photon energy of 30 eV. Figure 1(a) exhibits the population of the initial state for the parallel geometry at various peak intensities (I_0) between 10^{12} and 10^{14} W/cm^2 through $1-P_{\rm surv}(t)$, while Fig. 1(b) displays the alignment effect on $P_{\rm surv}(t)$ at a fixed peak intensity of 10^{14} W/cm^2. We see that the largest depletion occurs in the most tilted geometry ($\theta_N = 90°$). The dependence of $P_{\rm surv}(t)$ on the alignment angle observed here at $\hbar\omega = 30$ eV is very similar to that for 75 eV [6]. This is not surprising, as both photon energies fall into the xuv regime. A similar behavior is observed for the H_2^+ ion. The closer the alignment angle moves toward 90°, the lower is the survival probability. This is a common feature for photoionization by xuv radiation, whose mechanism differs considerably from that in the infrared regime [18]. Even in the perpendicular geometry, the survival probability at the end of the time propagation is about 0.966. Hence the depletion of the initial state is still negligible.

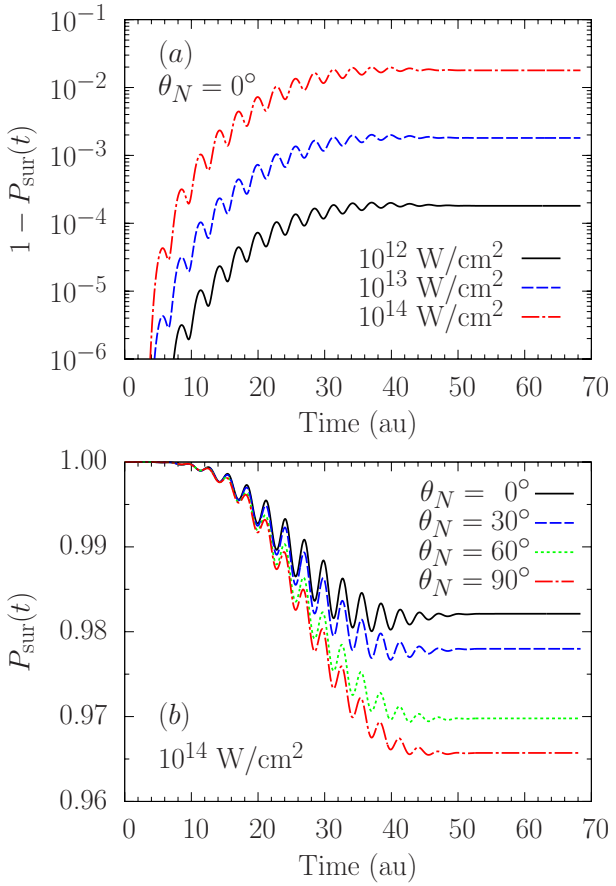

FIG. 1. (Color online) Survival probability of the H_2 molecule subjected to a sine-squared laser pulse with a central photon energy of 30 eV: (a) $\theta_N = 0°$ and $I_0 = 10^{12}$, 10^{13}, and 10^{14} W/cm^2; (b) $\theta_N = 0°$, 30°, 60°, and 90° with $I_0 = 10^{14}$ W/cm^2. The time duration is 10 optical cycles followed by 2 cycles of field-free propagation. The timescale is given in atomic units.

B. TDCS for arbitrary alignment

We now explore the angle-resolved cross sections in the coplanar configuration, i.e., in the plane formed by the molecular axis and the laser polarization axis, for equal energy sharing. Note that the angles of the two ejected electrons, θ_1 and θ_2, are measured with respect to the $\boldsymbol{\epsilon}$ vector rather than in the molecular body frame. In our calculations, no intensity effect is observed within the thickness of the lines (not shown) when we increase I_0 from 10^{12} to 10^{13} and finally to 10^{14} W/cm^2. In what follows, we therefore use a peak intensity of 10^{14} W/cm^2 to depict the alignment effect in the TDCSs.

Figures 2, 3, 4, and 5 display the alignment dependence of the angular distributions at equal energy sharing on the molecular orientation for the fixed electron detected at $\theta_1 = 0°$, 30°, 60°, and 90°, respectively. Overall, the magnitude of the generalized cross section in the perpendicular geometry is about $5-15$ times larger than that for the parallel case. Interestingly, the open Π_g channel does not introduce significantly new patterns compared to what we obtained for the geometries of $\theta_N = 0°$ and 90°. The angular distributions essentially show either the one- or two-lobe structure, with the details depending on the direction of $\boldsymbol{k}_1$.

If the fixed reference electron is observed along the direction of the polarization vector, the angular distributions are symmetric with respect to that direction only in the particular cases of $\theta_N = 0°$ and 90° [c.f. Figs. 2(a) and 2(j)], or if the fixed electron is detected exactly perpendicular to $\boldsymbol{\epsilon}$ [c.f. Figs. 5(a) and 5(j)]. The back-to-back emission mode, where $\theta_{12} = 180°$, is the characteristic feature for these configurations. This symmetry apparently breaks down for other values of the observation angle θ_1 and also for all other alignment geometries ($\theta_N \neq 0°$ and $\theta_N \neq 90°$). For the same direction of the reference electron and increasing alignment angle until $\theta_N \lesssim 30°$, the dominant peak for backward emission (θ_2) broadens and moves toward the molecular axis. When the alignment angle is between 30° and 50°, however, the shape of the emission mode remains relatively stable, although the magnitudes of the TDCSs are smoothly reduced. Moreover, when θ_N increases further toward 90°, the second electron is preferably emitted in the opposite direction to the reference electron. Then it recovers the back-to-back emission mode at $\theta_N = 90°$, which essentially corresponds to a single-lobe structure.

When the first electron is not observed along the polarization direction (c.f. Figs. 3, 4, and 5), the emission

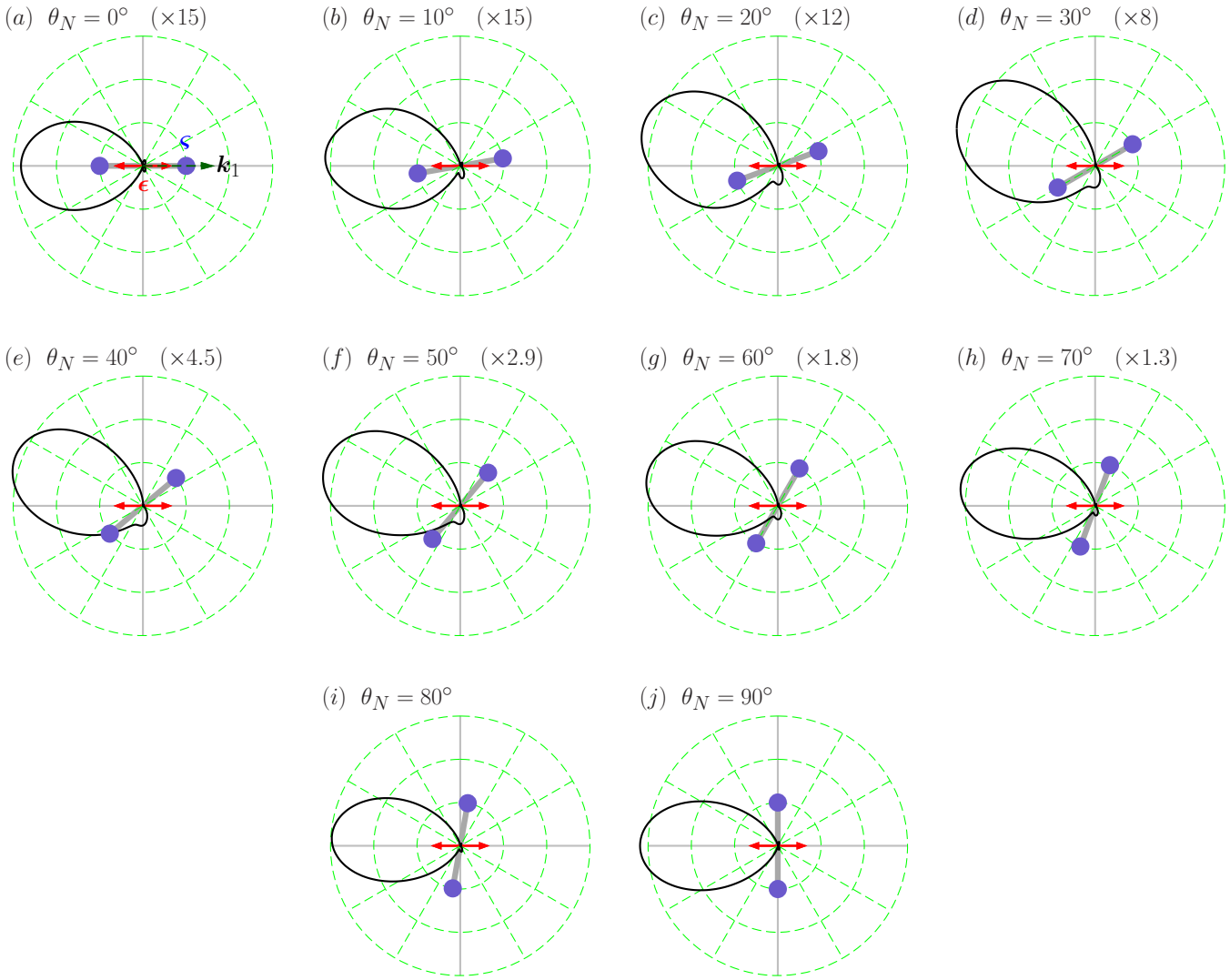

FIG. 2. (Color online) Dependence of the coplanar angular distribution for two-photon double ionization of H_2 on the orientation (θ_N) of the molecular axis ($\boldsymbol{\varsigma}$) with respect to the laser polarization vector ($\boldsymbol{\epsilon}$). The two ejected electrons share the excess energy equally, i.e., $E_1 = E_2 = 4.3$ eV. For a variety of molecular orientations, the fixed (reference) electron is observed along the direction $\boldsymbol{k}_1$, which is parallel to the $\boldsymbol{\epsilon}$ vector. The scale factors for $0° \leq \theta_N \leq 90°$ listed in the corresponding panels are used to bring the results for all geometries on the same scale. The radius of the outer circle corresponds to 3×10^{-54} cm^{4}s.

mode with the two-lobe feature cannot be neglected. In these geometries, the two correlated photoelectrons are ejected in a more complicated pattern. There are dramatic changes in the ejection modes compared to the cases of $\boldsymbol{k}_1$ parallel to $\boldsymbol{\epsilon}$. In these cases, the negligibly small lobe for $\boldsymbol{k}_1 \parallel \boldsymbol{\epsilon}$ develops considerably (c.f. Fig. 3), and even becomes one of the dominant peaks (c.f. Figs. 4 and 5) in the angular distributions. The shapes and relative magnitudes of the two-peak structure are very sensitive to the alignment angle. This is seen, for example, in the case of $\theta_1 = 60°$.

The present analysis allows us to predict the dominant patterns to be expected in experimental observations of the angular distributions from the two-photon process, which we hope will be carried out in the foreseeable future. Even in the measurements of single-photon double ionization in H_2, there are significant uncertainties in the alignment angles and the acceptance angles of the reference electron. Typically, they can be as large as $\pm 20°$ or $\pm 30°$. It seems reasonable to assume similar acceptance angles θ_N and θ_1 for future two-photon breakup measurements. To simplify the discussion, however, we will now concentrate on cases, in which only one of these angles (θ_N or θ_1) has a significant uncertainty.

Let us discuss, for example, the effect of an uncertainty in θ_N on the shape of the angular distributions. In the case of $\boldsymbol{\zeta}$ orientated around $\boldsymbol{\epsilon}$ (e.g., $\theta_N = 0° \pm 30°$) and $\boldsymbol{k}_1 \parallel \boldsymbol{\epsilon}$, the large magnitude differences at various θ_N will cause the observed pattern in the angular distribution to be dominated by contributions from the larger values of θ_N. This will likely lead to a noticeably broader two-lobe emission mode rather than the single-lobe structure

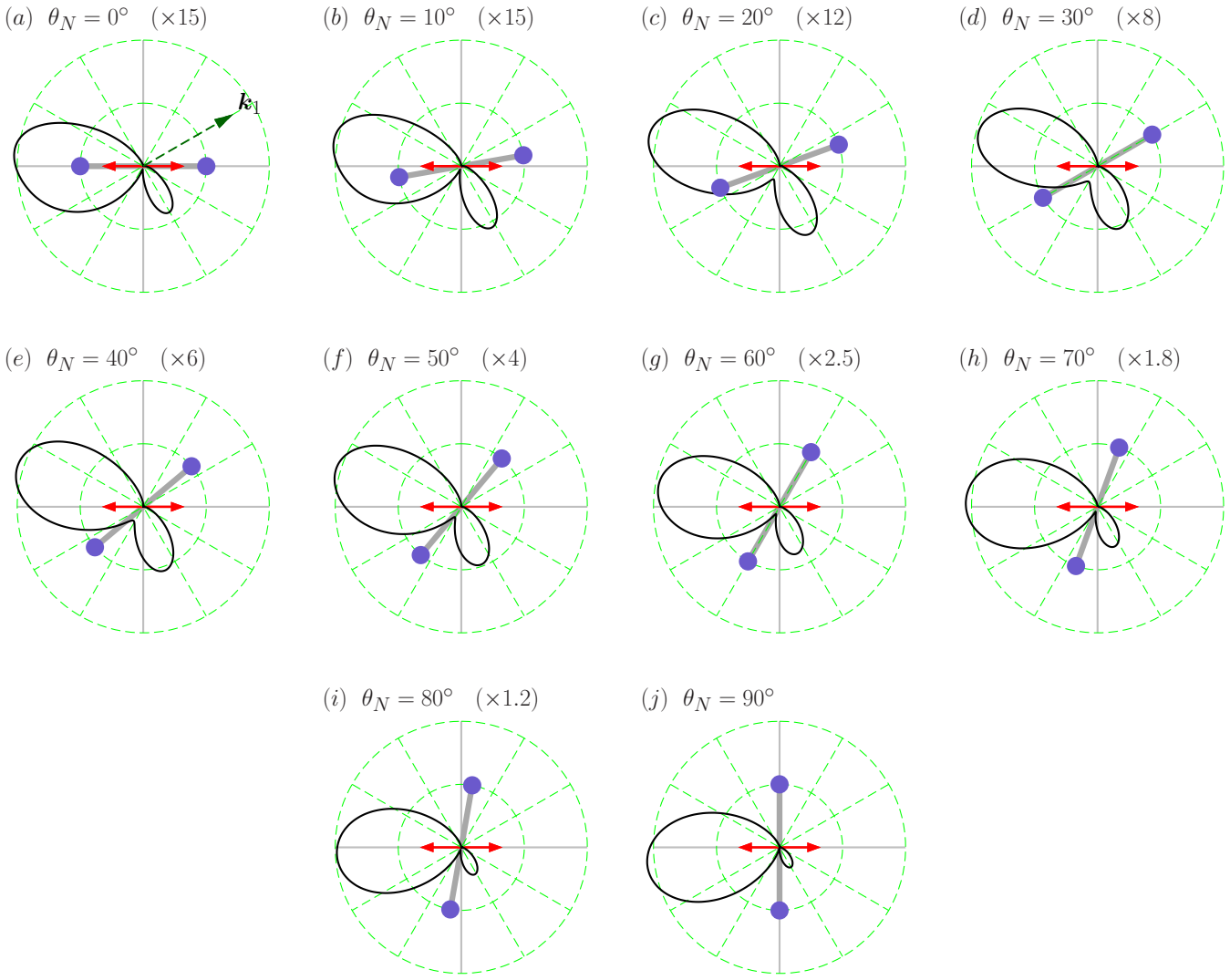

FIG. 3. (Color online) Same as Fig. 2, except that the reference electron is detected at $\theta_1 = 30°$.

predicted for the pure parallel geometry. On the other hand, when we turn to the case of $\theta_N \approx 90°$, the situation flips around, because the $\theta_N = 90°$ geometry is already the dominant mode compared to its neighbors. Hence, modulations in the width of the lobe may not be as obvious in this case as in the parallel geometry.

We conclude that the alignment effect of the molecular axis with respect the polarization vector is more apparent for small orientation angles, where $\boldsymbol{\zeta}$ is nearly parallel to $\boldsymbol{\epsilon}$. In this respect, the two-photon double ionization is similar to that of single-photon double ionization in the hydrogen molecule. However, we should recall the pronounced distinction between the cases of one- and two-photon double ionization. In the former, the alignment deviation from the parallel geometry has a strong effect on the angular distribution. In fact, the experimental uncertainty in the angle θ_N can even change the dominant mode from forward emission to backward emission [3, 5]. In the two-photon case, on the other hand, no such dramatic conversion is observed.

Furthermore, the predicted angular distributions are very sensitive to the direction of $\boldsymbol{k}_1$. For $\theta_1 = 90°$ and θ_N centered around 90° (e.g., $\theta_N = 90° \pm 30°$), the two-lobe backward scattering mode should be observed, thus resembling the shape of the pure $\theta_N = 90°$ geometry. From Fig. 5, however, we see that this mode should be attributed to the geometry of $\theta_N = 60°$, due to the large magnitude of its TDCS. The intricate details of these modulated angular distributions will lead to a strong dependence of the observed signal on the detector acceptance angles of the molecular axis and the directions of the photoelectrons. These would have to be known in detail and incorporated properly in a numerical simulation of the experiment.

In addition to the uncertainties in the electron detection and the alignment angles, the angular distributions are potentially sensitive to the internuclear separation where the nonsequential double photoionization actually

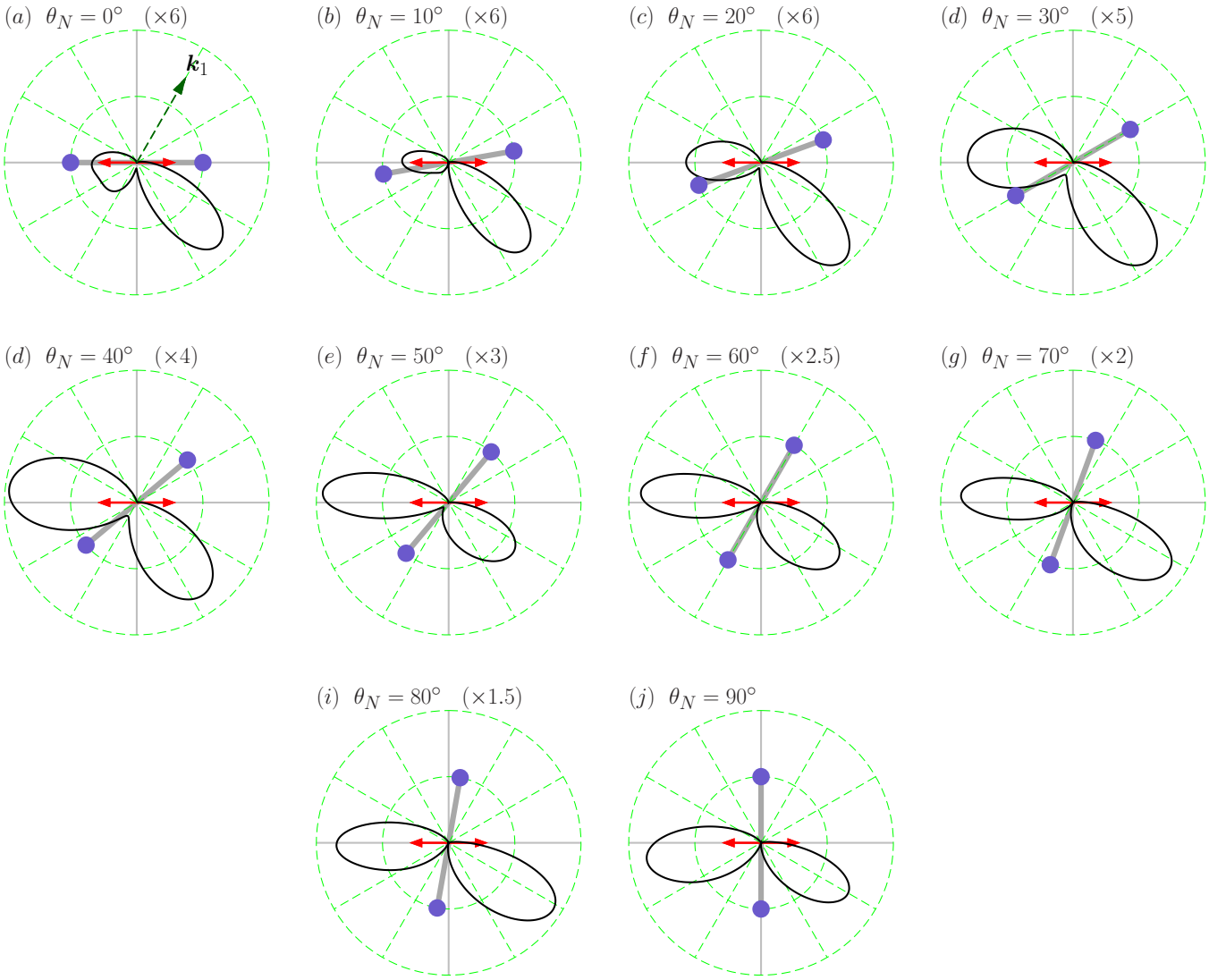

FIG. 4. (Color online) Same as Fig. 2, except for $\theta_1 = 60°$.

happens. Comparing the parallel and perpendicular geometries, a previous study [8] indicated that the parallel geometry exhibits a higher sensitivity of both the magnitude and the shape of the calculated TDCSs when reducing the internuclear separation to 1.2 bohr or increasing it to 1.6 bohr. The parallel geometry thus shows a stronger molecular effect than the perpendicular case when the internuclear separation is varied.

Although a detailed study of the dynamical effects of the nuclear motion are very interesting, both the theoretical and computational tools required for such a study are not in hand at this time. We are, however, already in the process of developing these methods, in order to be prepared once the required computational resources become available. Here we concentrate on varying just one (θ_N) instead of both (θ_N and R) parameters at fixed $R = 1.4$ bohr, with the principal goal of providing theoretical benchmark results for future studies of this process. While certainly a restriction on generality, this approach enables us to thoroughly consider an already intricate problem.

Next, we analyze the relative contributions from the individual channels and the effects of their interference. Figures 6 and 7 depict the contributions to the total TDCSs from the ionization channels Σ_g, Π_g, Δ_g, as well as that from the interference terms, at selected alignment geometries ($\theta_N = 10°$, $30°$, $40°$, $60°$, $70°$, and $90°$). The reference electron is detected at $\theta_1 = 0°$ (Fig. 6) or $90°$ (Fig. 7), respectively. Overall, we see dramatic changes in the channel contributions when the molecular alignment varies.

A few features should be noticed. For $\theta_1 = 0°$, for example, the Δ_g channel only plays a role for sufficiently large values of θ_N ($\gtrsim 60°$) and can be safely neglected at smaller θ_N. Interestingly, for $\theta_N \gtrsim 60°$, the shape and magnitude of the pure Σ_g and Δ_g contributions are very similar. Meanwhile, the role of the Π_g channel fades off gradually in this region of θ_N values, before it completely

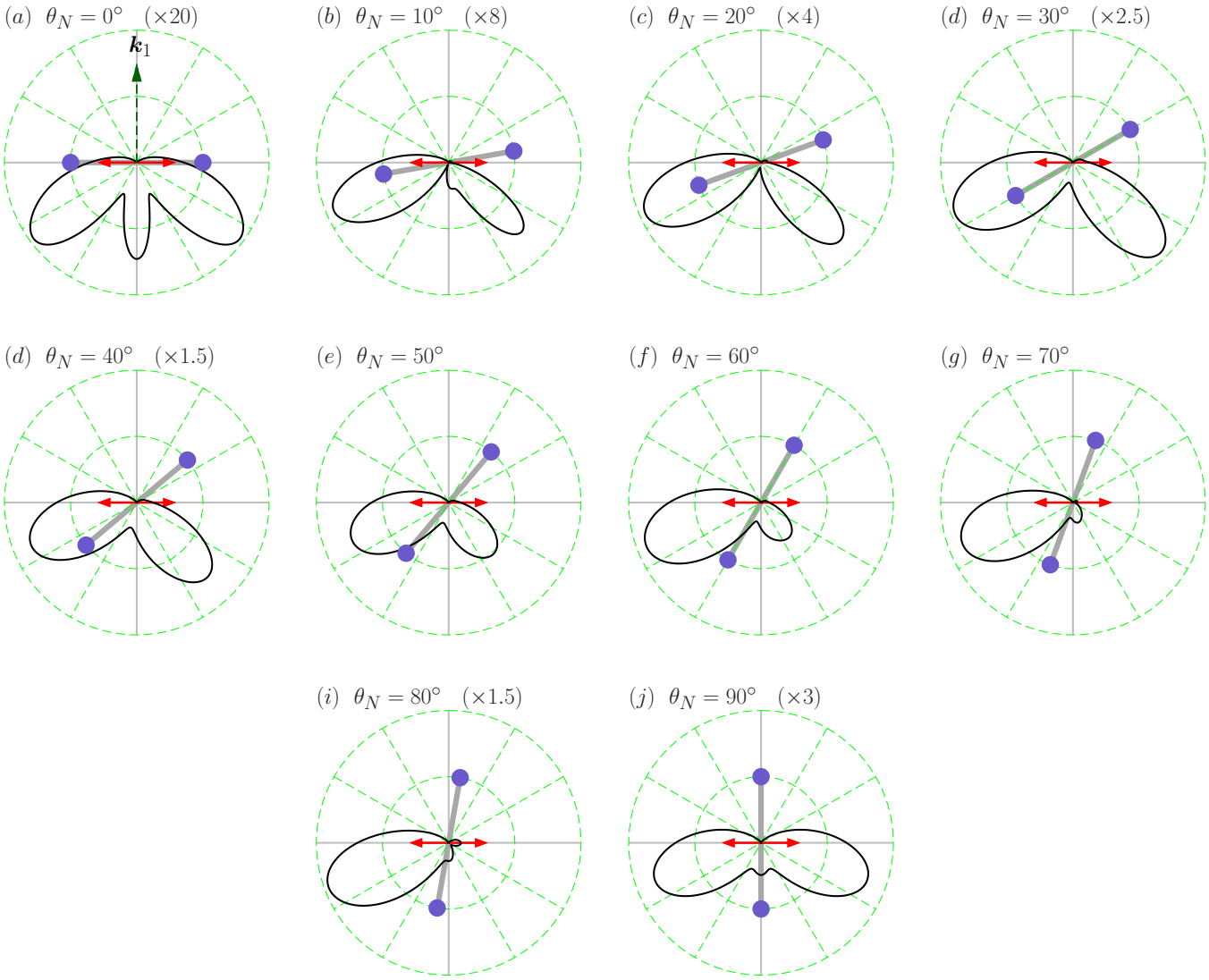

FIG. 5. (Color online) Same as Fig. 2, except for $\theta_1 = 90°$.

vanishes at $\theta_N = 90°$.

At small alignment angles ($\theta_N \lesssim 10°$), the dominant single-lobe structure originates from the Σ_g channel. Also, the interference contribution is small but not entirely negligible. This result makes sense, since the perpendicular component of the electric field is weak for small θ_N.

The Δ_g channel can only be populated through $\Sigma_g \xrightarrow{\perp} \Pi_u \xrightarrow{\perp} \Delta_g$. This is different from the situation for the final Π_g channel, where both the parallel and perpendicular components of the electric field are contributing. Furthermore, at small values of θ_N, the interference between the channels can be either constructive or destructive in building up the TDCS results. This interference term mostly originates from the Σ_g and Π_g channels. When θ_N is large, the interference term generally makes a significant constructive contribution to the cross sections. It can even be larger than the individual contribution from the Σ_g or Δ_g channels. Note that the interference term only depends on the magnitudes of the ionization amplitudes in the channels involved, but it is also sensitive to their relative phase differences. This results in either constructive or destructive contributions to the TDCSs. The single-lobe peak in the TDCSs is significantly enhanced by the constructive interference effect. As we stressed before, at the fixed direction of $\theta_1 = 0°$, only a single dominant lobe oscillates for θ_2 between about 160° and 180° when θ_N varies from 0° to 90°. However, this single lobe exhibits a completely different angular symmetry, for example, at $\theta_N = 0°$ and 90°.

Figure 7 exhibits the channel contributions for the reference electron observed at $\theta_1 = 90°$. In this case, some of the observations described for $\theta_1 = 0°$ no longer hold. We first notice that the contribution from the Δ_g channel for small alignment angles is (relatively) much larger than in the case of $\theta_1 = 0°$. Secondly, over a wide range of θ_N, the interference term provides a mostly destructive

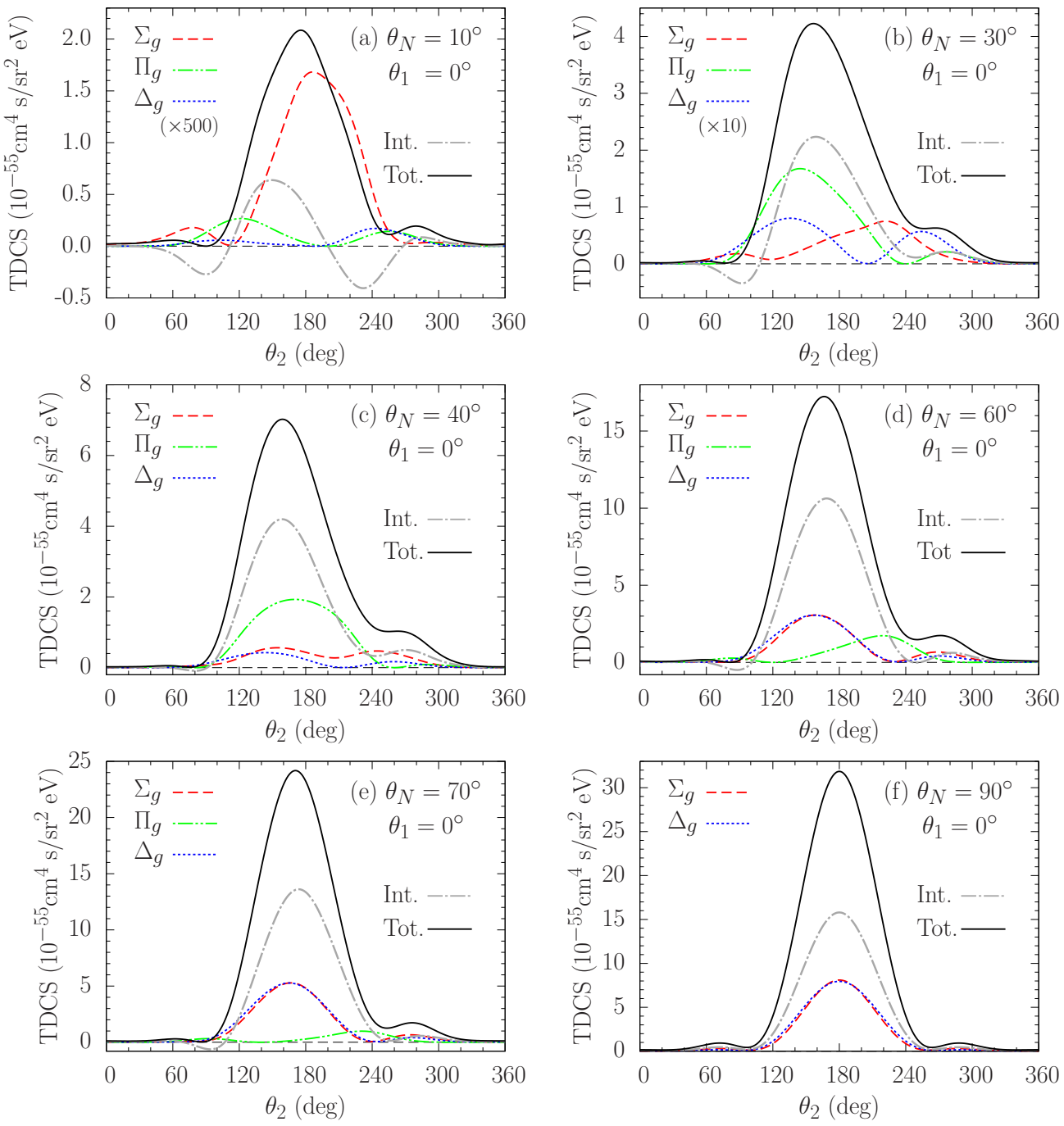

FIG. 6. (Color online) Channel and interference (Int.) contributions to the total (Tot.) TDCS for the reference electron observed at $\theta_1 = 0°$.

contribution to the TDCS results. In most cases, the Π_g contribution is canceled by the interference effect. This results in either a minimum [c.f. Figs. 7(b) and (c)] or a reduced amplitude of the second lobe [c.f. Figs. 7(d) and (e)]. Only at $\theta_N = 90°$ the interference effect contributes to the TDCS in a constructive way.

From the above discussion, we clearly see an alignment effect for the TDCSs of molecular hydrogen. Nevertheless, it seems worth investigating to what extent the TDCS patterns seen in the H_2 molecule resemble those of its atomic counterpart, the helium atom. In Fig. 8, we display a detailed comparison between the coplanar TDCSs for the H_2 and He targets at equal energy sharing. Among the various alignment geometries, not surprisingly, the angular distributions of H_2 in the perpendicular geometry ($\theta_N = 90°$) resemble most closely those

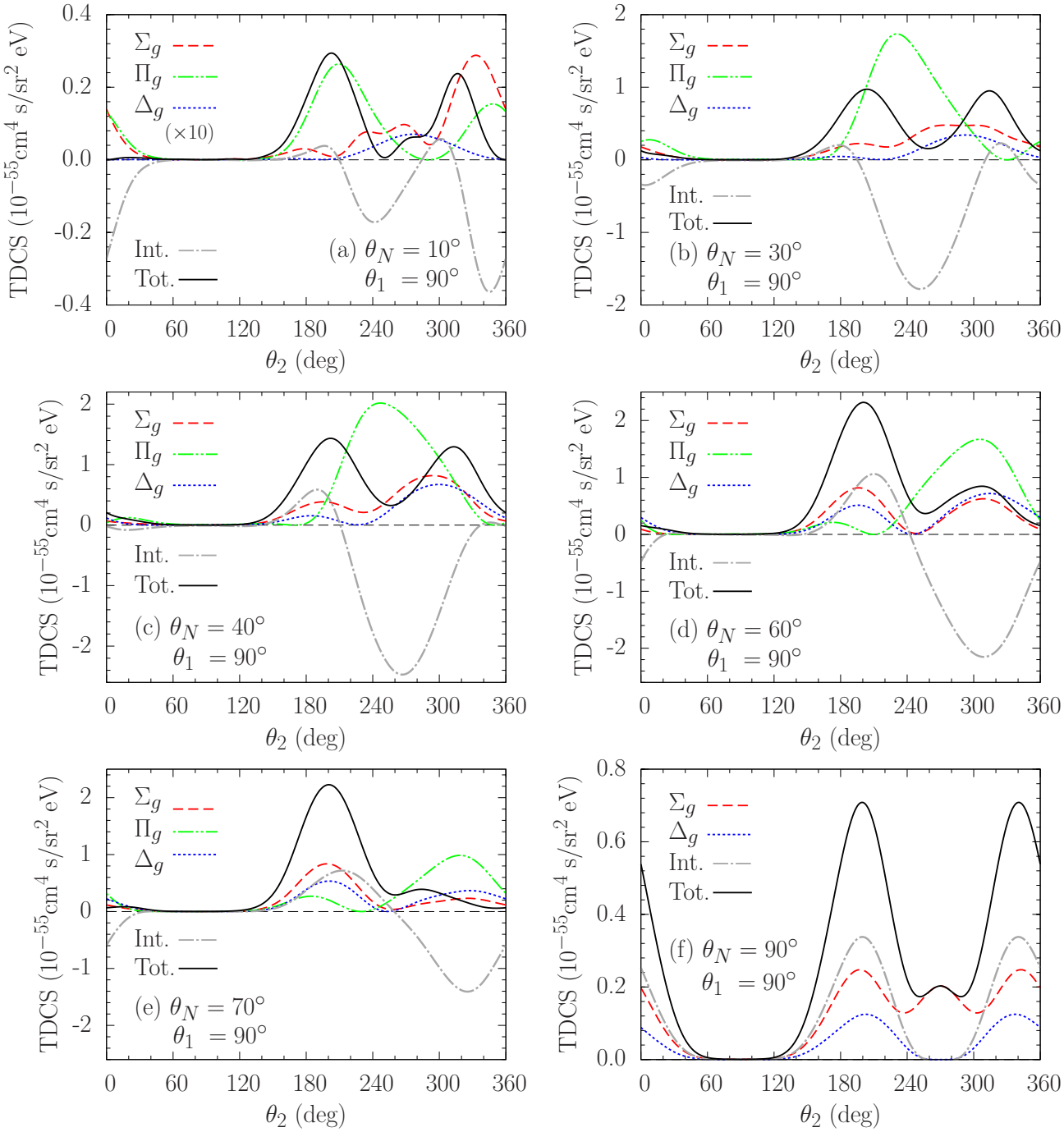

FIG. 7. (Color online) Same as Fig. 6, except that the reference electron is observed at $\theta_1 = 90°$.

for the helium atom. Although the total magnetic quantum number along the molecular axis is not conserved in the case of $\theta_N = 90°$, only this perpendicular geometry shows similar transition paths as the helium atom. The selection rule ${}^1\Sigma_g \to {}^1\Pi_u \to ({}^1\Sigma_g, {}^1\Delta_g)$ in H_2 is similar to ${}^1S \to {}^1P^o \to ({}^1S, {}^1D)$ in helium.

Other geometries, either by mixing with the ${}^1\Pi_g$ channel or by having the ${}^1\Sigma_g$ channel alone, result in major deviations from the one-center atomic target. In terms of the magnitudes and shapes of the predicted TDCSs, we further observe that dividing the H_2 TDCS at $\theta_N = 90°$ by a about 3.5 brings the numerical values into fairly good agreement with those for the helium atom. Interestingly, this scale factor is apparently rather insensitive to the direction of the reference electron.

This finding suggests that the total cross section ($\sigma_{\rm tot}$) for double ionization of H_2 at the photon energy of 30 eV may be estimated from that of the helium atom at the

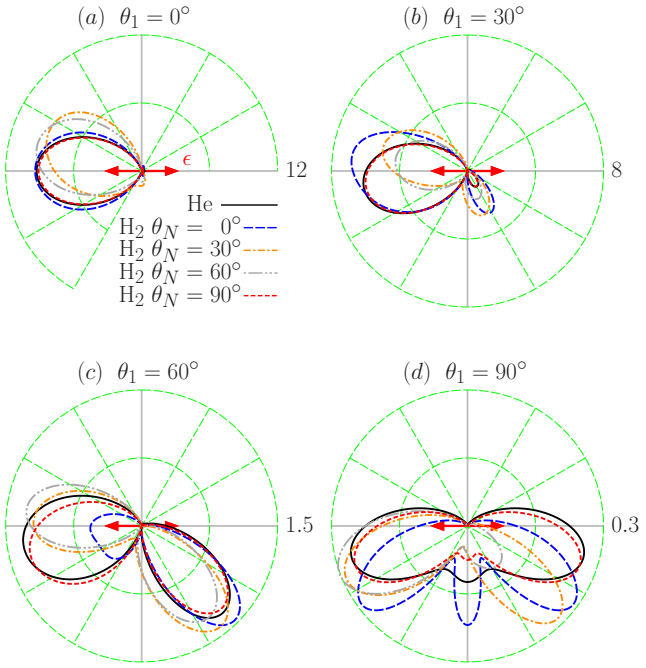

FIG. 8. (Color online) Angular distributions for two-photon double ionization of the hydrogen molecule and the helium atom at equal energy sharing. The central photon energies for H_2 and He are 30 and 42 eV, respectively. The polarization vector of the laser pulse is along the horizontal direction. The labels (12, 8, 1.5, and 0.3) in each panel indicate the radius of the outer circle in units of 10^{-55} cm^{4}s. The H_2 TDCSs were multiplied by scale factors in order to bring the angular distributions on the same scale as those for the helium atom. Hence, only the shape of the H_2 distributions should be compared to those for the helium atom, for which the absolute numbers apply.

photon energy of 42 eV. The latter was predicted as $\sigma_{\rm tot} = 3.93 \times 10^{-53}$ cm^{4}s [22]. For an angle-independent scale factor, the same ratio would apply to the single-differential cross section (SDCS) with respect to the energy of the reference electron, $d\sigma/dE_1$. Since the total cross section is obtained from the SDCS by integrating the latter over the possible values of E_1, we need to introduce a factor of $8.6/5.0 \approx 1.7$ to account for the different excess energies (5.0 eV for helium and 8.6 eV for H_2). We then obtain $\sigma_{\rm tot} \approx 2.4 \times 10^{-52}$ cm^{4}s for H_2 at 30 eV. The accurate numerical result, obtained after numerically integrating over the possible energy sharings, is 2.6×10^{-52} cm^{4}s. This minor (7%) difference is partly due to the approximation of a flat energy dependence of $d\sigma/dE_1$. In reality, the SDCS is often a little higher at highly asymmetric energy sharing ($E_1 \simeq 0$ or $E_1 \simeq E_{\rm exc}$) than near equal energy sharing. Consequently, we slightly underestimated the total cross section using the above rule-of-thumb procedure. Nevertheless, this approximation may be useful for experimentalists in order to quickly estimate the relative contributions from various channels that may be expected in a particular measurement.

V. SUMMARY

We have presented a detailed analysis of the angle-resolved triple-differential cross section for two-photon double ionization of the aligned hydrogen molecule at a central photon energy of 30 eV by solving the time-dependent Schrödinger equation in an FE-DVR approach. The internuclear separation was fixed at its equilibrium distance of 1.4 bohr. The alignment angle θ_N was uniformly increased from 0° to 90° in steps of 10° in the FNA. The two photoelectrons share the excess energy of 8.6 eV equally. Our analysis of the dependence of the predicted TDCS on the relative orientation between the molecular axis and the polarization vector suggests that in the intermediate cases (where θ_N is neither 0° nor 90°) the appearance of the Π_g channel does not significantly alter the shape of the angular distributions. We found, however, that the relative magnitudes of the two-peak patterns can be very sensitive to the alignment angle. In light of the expected large experimental acceptance angles (for both θ_1 and θ_N), we expect the present investigation to be useful for planning future measurements on two-photon double ionization of diatomic molecules.

ACKNOWLEDGMENTS

This work was supported by the NSF under grant PHY-0757755 (XG and KB) and supercomputer resources through the TeraGrid allocation TG-PHY090031 (Kraken at NICS, Oak Ridge National Laboratory). We also gratefully acknowledge support from the Department of Energy through the allocation award MPH006 (Jaguar at NCCS, Oak Ridge National Laboratory).

[1] Th. Weber, A. Czasch, O. Jagutzki, A. Müller, V. Mergel, A. Kheifets, J. Feagin, E. Rotenberg, G. Meigs, M. H. Prior, S. Daveau, A. L. Landers, C. L. Cocke, T. Osipov, H. Schmidt-Böcking, and R. Dörner, Phys. Rev. Lett. **92** 163001 (2004).

[2] T. Weber, A. Czasch, O. Jagutzki, A. Müller, V. Mergel, A. Kheifets, E. Rotenberg, G. Meigs, M. H. Prior, S. Daveau, A. L. Landers, C. L. Cocke, T. Osipov, R. Díez Muiño, H. Schmidt-Böcking, and R. Dörner, Nature (London) **431**, 437 (2004).

[3] M. Gisselbrecht, M. Lavollée, A. Huetz, P. Bolognesi, L. Avaldi, D. P. Seccombe, and T. J. Reddish, Phys. Rev. **96**, 153002 (2006).

[4] W. Vanroose, D. A. Horner, F. Martín, T. N. Rescigno, and C. W. McCurdy, Phys. Rev. A **74**, 052702 (2006).

[5] J. Colgan, M. S. Pindzola, F. Robicheaux, Phys. Rev. Lett. **98**, 153001 (2007).
[6] X. Guan, K. Bartschat, and B. I. Schneider, Phys. Rev. A **83**, 043403 (2011).
[7] Y. H. Jiang, A. Rudenko, E. Plésiat, L. Foucar, M. Kurka, K. U. Kühnel, Th. Ergler, J. F. Pérez-Torres, F. Martín, O. Herrwerth, M. Lezius, M. F. Kling, J. Titze, T. Jahnke, R. Dörner, J. L. Sanz-Vicario, M. Schöffler, J. van Tilborg, A. Belkacem, K. Ueda, T. J. M. Zouros, S. Düsterer, R. Treusch, C. D. Schröter, R. Moshammer, and J. Ullrich, Phys. Rev. A **81**, 021401(R) (2010).
[8] J. Colgan, M. S. Pindzola, and F. Robicheaux, J. Phys. B **41**, 121002 (2008).
[9] F. Morales, F. Martín, D. A. Horner, T. N. Rescigno, and C. W. McCurdy, J. Phys. B **42**, 134013 (2009).
[10] X. Guan, K. Bartschat, and B. I. Schneider, Phys. Rev. A **82**, 041404(R) (2010).
[11] T.-G. Lee, M. S. Pindzola, and F. Robicheaux, J. Phys. B **43**, 165601 (2010).
[12] D. R. Bates, U. Öpik, and G. Poots, Proc. Phys. Soc. A **66**, 1113 (1953).
[13] L. Tao, C. W. McCurdy, and T. N. Rescigno, Phys. Rev. A **82**, 023423 (2010).
[14] S. Barmaki, S. Laulan, H. Bachau, and M. Ghalim, J. Phys. B **36**, 817 (2003).
[15] S. Barmaki, H. Bachau, and M. Ghalim, Phys. Rev. A **69**, 043403 (2004).
[16] G. Lagmago Kamta and A. D. Bandrauk, Phys. Rev. A **71**, 053407 (2005).
[17] L. Tao, C. W. McCurdy, and T. N. Rescigno, Phys. Rev. A **79**, 012719 (2009).
[18] Y. V. Vanne and A. Saenz, Phys. Rev. A **82**, 011403(R) (2010).
[19] K. Sakimoto, Phys. Rev. A **71**, 062704 (2005).
[20] F. Robicheaux, J. Phys. B **29**, 779 (1996).
[21] X. Guan and K. Bartschat, Phys. Rev. Lett. **103**, 213201 (2009).
[22] X. Guan, K. Bartschat, and B. I. Schneider, Phys. Rev. A **77**, 043421 (2008).